In-plane electron-phonon coupling anisotropy and multiple charge density wave orders in the superconductor $Bi_2Rh_3Se_2$

Yongsong Wang,[1] Bo Chen,[1] Zi-Teng Liu,[1] Xiao Guo,[1] Siwen You,[1] Zihan Wang,[1] Haipeng Xie,[1] Tianchao Niu,[2] Jian-Qiao Meng,[1,*] and Han Huang[1,†]

[1]*School of Physics and Electronics, Hunan Key Laboratory of Super-microstructure and Ultrafast Process, Central South University, 932 South Lushan Road, Changsha, Hunan 410083, People's Republic of China*

[2]*Beihang Hangzhou Innovation Institute Yuhang, Xixi Octagon City, Yuhang District, Hangzhou 310023, China*

(Received 15 November 2022; revised 13 June 2023; accepted 20 June 2023; published 12 July 2023)

The ternary chalcogenide superconductor $Bi_2Rh_3Se_2$ was discovered to have charge density wave (CDW) order and electron-phonon coupling (EPC). However, it is still debated whether the phase transition at ∼240 K is a CDW one. Here, we systematically performed Raman scattering investigations on single-crystal $Bi_2Rh_3Se_2$. Angle-resolved polarized Raman spectroscopic measurements reveal the in-plane anisotropic EPC in $Bi_2Rh_3Se_2$, which inhibits the Raman intensity. Temperature-dependent x-ray diffraction and Raman measurements indicate the existence of the incommensurate (ICCDW) and commensurate (CCDW) CDW orders below ∼250 and ∼170 K, respectively, in $Bi_2Rh_3Se_2$. The appearance of zone-folded phonon modes at ∼170 K confirms the CCDW-induced 2×2 reconstruction of the Brillouin zone. Semiquantitative analysis based on Landau theory of second-order phase transitions of CDW-correlated and uncorrelated phonon modes reflects extensive coupling between the phonons and CDW orders. Our findings elucidate the existence of CCDW and ICCDW and confirm the critical role of EPC in CDW transitions in $Bi_2Rh_3Se_2$.

DOI: 10.1103/PhysRevB.108.045118

I. INTRODUCTION

Charge density wave (CDW) and superconductivity are two very important and closely linked collective excitations in solids, and their interactions have been investigated widely [1–4]. BCS superconducting theory [5] and the CDW formation mechanism [6,7] point out that both superconductivity and CDW order originate from electron-phonon coupling (EPC) and compete with each other. However, recent investigations on $2H-NbSe_2$ demonstrate that CDW order does not simply compete with superconductivity [8]. There is increasing evidence for CDW order existing in high-T_c cuprate superconductors [1,3,9,10]. The competition or coexistence relationship between CDW and high-T_c superconductivity remains unclear and deserves more in-depth investigations.

$Bi_2Rh_3Se_2$ offers a potential platform to investigate the interaction between CDW order and superconductivity, since it is reported to exhibit a superconducting transition at $T_c \sim 0.7$ K and a CDW order below $T_s \sim 240$ K [11–13]. Measurements such as electrical resistivity, specific heat, and temperature-dependent x-ray diffraction (TDXRD) [11] as well as optical conductivity [12] and angle-resolved photoelectron spectroscopy (ARPES) [13] suggest that the phase transition at ∼240 K is a CDW one, showing evidence of EPC [12,13]. However, pressure-dependent electrical resistivity measurements illustrate an unexpected rise in anomaly temperature with pressure. Moreover, temperature-dependent selected-area electron diffraction (SAED) measurements demonstrate that it is a purely structural transition [14]. Thus, disclosing whether the phase transition at ∼240 K is a CDW one or a purely structural one is the first and most essential step. Raman spectroscopy is an effective method to investigate the physical properties such as EPC and phase transitions: Angle-resolved polarized Raman spectroscopy (ARPRS) can reveal the in-plane anisotropy [15,16], and temperature-dependent Raman spectroscopy (TDRS) can unveil the phonon anharmonicity, purely structural phase transition, as well as second-order phase transitions, such as CDW and magnetic phase transitions, etc. [17–34].

In this work, we report on the systematic Raman scattering investigations on single crystalline $Bi_2Rh_3Se_2$. XRD, scanning electron microscopy (SEM), and high-resolution transmission electron microscopy (HRTEM) measurements have been carried out to demonstrate the high quality of the as-grown $Bi_2Rh_3Se_2$ crystals. ARPRS measurements reveal the in-plane phonon and EPC anisotropies. An excitation wavelength-dependent EPC is also observed. TDRS combined with TDXRD measurements from 80 to 300 K disclose two distinct second-order phase transitions at $\sim 170 \pm 10$ K (T_1) and $\sim 250 \pm 10$ K (T_2, close to T_s) in $Bi_2Rh_3Se_2$, respectively. The reversible appearance and disappearance of zone-folded phonon modes provide clear evidence of the Brillouin zone (BZ) reconstruction following CCDW transition at ∼170 K. Quantitative analysis of the evolution of peak frequencies and intensities with temperature shows an interaction between phonons and CDWs. Our findings demonstrate the worth and urgency of further studies of CDWs and their interactions with superconductivity in $Bi_2Rh_3Se_2$.

*jqmeng@csu.edu.cn
†physhh@csu.edu.cn

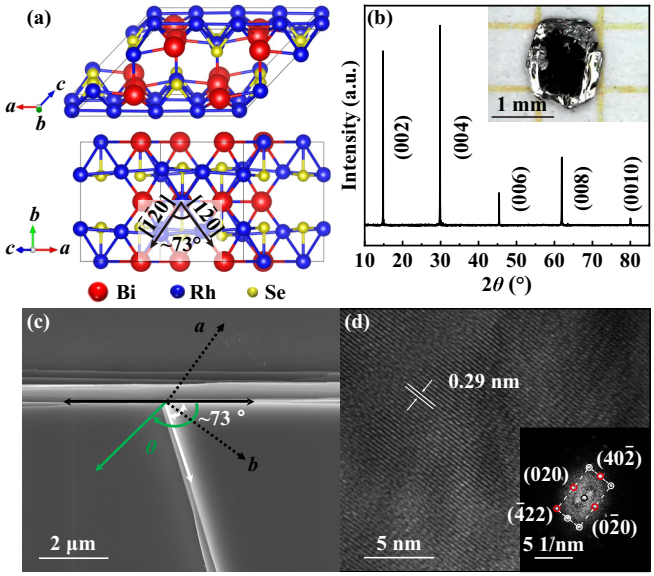

FIG. 1. (a) Crystal structure of $Bi_2Rh_3Se_2$. (b) XRD pattern of as-grown $Bi_2Rh_3Se_2$ crystal. The inserted optical image shows the $Bi_2Rh_3Se_2$ crystal in a millimeter-scale. (c) SEM image of a freshly cleaved $Bi_2Rh_3Se_2$ crystal. Black dotted arrows present crystallographic *a*- and *b*- axes. (d) HRTEM image of an exfoliated $Bi_2Rh_3Se_2$ flake. The inset shows the corresponding fast Fourier transform pattern.

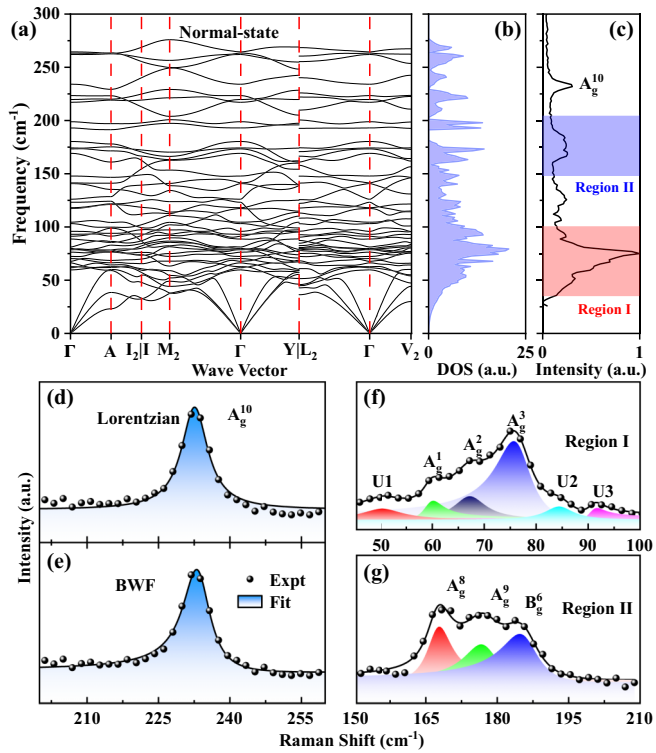

FIG. 2. Calculated phonon dispersion (a) and the corresponding DOS (b) of normal-state $Bi_2Rh_3Se_2$. (c) Raman spectrum of as-grown $Bi_2Rh_3Se_2$ crystals under 532 nm excitation at 300 K. A_g^{10} mode performed by Lorentzian (d) and BWF functions (e). Raman-active modes in regions I (f) and II (g).

II. RESULTS AND DISCUSSION

Normal-state bulk $Bi_2Rh_3Se_2$ with a space group $C12/m1$ has the parkerite-type structure with standardized unit-cell parameters of $a = 1.141$ nm, $b = 0.837$ nm, $c = 0.822$ nm, and $\beta = 133.148°$ [35], as schematically shown in Fig. 1(a). Rh atoms (blue) are covalently bonded with Se (yellow), Bi (red), and Rh atoms to form anisotropic pseudo-two-dimensional networks, implying there possibly exists anisotropic properties in $Bi_2Rh_3Se_2$ [11,14]. The room-temperature XRD pattern of the millimeter-scale as-grown $Bi_2Rh_3Se_2$ crystals (optical image inserted) shown in Fig. 1(b) only displays five intense peaks at $2\theta = 14.84°$, $29.86°$, $45.42°$, $61.94°$, and $80.04°$, in good agreement with previous reports [11]. The interplanar spacing corresponding to the first peak is calculated to be 1.193 nm, which matches well with $2 \times c \times \sin((180–133.148)°) = 1.199$ nm. Thus, the five peaks are assigned to (002), (004), (006), (008), and (0010) planes of $Bi_2Rh_3Se_2$, respectively, revealing that the as-grown $Bi_2Rh_3Se_2$ are single crystals. A representative SEM image on a freshly cleaved $Bi_2Rh_3Se_2$ flake in Fig. 1(c) shows an atomically smooth surface and long straight step edges, confirming the layered structure of $Bi_2Rh_3Se_2$. The angle included by the two long straight edges (marked by black and white solid arrows) is ~73° instead of 90° by vectors **a** and **b**, indicating that $Bi_2Rh_3Se_2$ crystals prefer to fracture along the $[\bar{1}\bar{2}0]$ and $[1\bar{2}0]$ directions [marked in Fig. 1(a)] rather than crystallographic *a*- and *b*-axes. Similar results have been reported in MoO_2 flakes [36,37]. A typical HRTEM image in Fig. 1(d) shows clear parallel stripes with an interplanar spacing of ~0.29 nm, consistent with a $a/4$ lattice constant of $Bi_2Rh_3Se_2$. The corresponding fast Fourier transform pattern inserted at the lower-right corner in Fig. 1(d) shows a rectangular symmetry and indicates that the first bright spot along the [100] direction corresponds to the $(40\bar{2})$ plane. For more details, see Fig. S1 in the supplemental material [38].

Figure 2(a) shows the calculated phonon dispersion of the normal-state $Bi_2Rh_3Se_2$ (for details, see the subsection that discusses DFPT calculations in Sec. IV), which exhibits real eigenvalues through all the high-symmetry points in the first BZ (the BZ of $Bi_2Rh_3Se_2$ is shown in Fig. S2 [38]), confirming its dynamical stability. At the Γ point, there are three acoustic and 39 optical phonon modes, whose calculated frequencies and symmetries are summarized in Table I. Among them, there are 10 A_g and 8 B_g Raman-active modes in 0–300 cm^{-1}. The corresponding density of states (DOS) is displayed in Fig. 2(b), extremely similar to the unpolarized Raman spectrum of as-grown $Bi_2Rh_3Se_2$ crystals under 532 nm excitation at 300 K in Fig. 2(c). The spectral ranges from ~50 to 100 and ~150 to 210 cm^{-1} are named regions I and II, respectively. The isolated peak at ~233 cm^{-1} is assigned to A_g^{10} mode (according to Table I).

A_g^{10} mode in Fig. 2(d) shows an asymmetric line shape and is performed poorly by the Lorentzian function (the coefficient of determination, R^2, is ~0.958). Similar asymmetric Raman line shapes have been observed in other superconductors and heavily *p*-doped semiconductor Si, all arising from Fano-type discrete-continuous resonances between phonons and electrons [17,18,22,23,39]. The modified Raman peak intensity (I) can be given by the Breit-Wigner-Fano (BWF)

TABLE I. Calculated frequencies and symmetries of phonon modes in $Bi_2Rh_3Se_2$.

Mode	A_g	A_u	B_g	B_u
Frequency (cm^{-1})	66.3(A_g^1)	0.1(A_u^1)	61.7(B_g^1)	−0.1(B_u^1)
	70.3(A_g^2)	59.7(A_u^2)	78.6(B_g^2)	0.1(B_u^2)
	76.3(A_g^3)	79.1(A_u^3)	79.6(B_g^3)	62.7(B_u^3)
	79.9(A_g^4)	88.7(A_u^4)	91.3(B_g^4)	67.7(B_u^4)
	93.1(A_g^5)	104.5(A_u^5)	126.1(B_g^5)	72.3(B_u^5)
	117.3(A_g^6)	123.2(A_u^6)	180.3(B_g^6)	81.2(B_u^6)
	140.8(A_g^7)	141.4(A_u^7)	217.2(B_g^7)	95.9(B_u^7)
	169.2(A_g^8)	193.0(A_u^8)	264.5(B_g^8)	103.2(B_u^8)
	174.2(A_g^9)	219.8(A_u^9)	/	118.1(B_u^9)
	234.1(A_g^{10})	262.0(A_u^{10})	/	147.9(B_u^{10})
	/	/	/	173.3(B_u^{11})
	/	/	/	198.8(B_u^{12})
	/	/	/	223.4(B_u^{13})
	/	/	/	263.3(B_u^{14})

function and written as [22,23,40]

$$I(\omega) = A\frac{[q + 2(\omega - \omega_0)/F]^2}{1 + [2(\omega - \omega_0)/F]^2}, \quad (1)$$

where A is the intensity parameter, ω_0 is renormalized phonon frequency, q is a parameter that quantitatively describes asymmetry, $1/q$ can describe EPC strength, and F is the full width at half-maximum (FWHM) parameter. As displayed in Fig. 2(e), A_g^{10} mode can be better described by the BWF function ($R^2 \sim 0.980$), and the extracted q is ~ -8.78, suggesting the existence of EPC in $Bi_2Rh_3Se_2$, as demonstrated in our previous report [13]. Then, six intense Raman-active modes with BWF line shapes shown in Figs. 2(f) and 2(g) were resolved at ∼60, 68, 75, 168, 178, and 185 cm^{-1} in regions I ($R^2 \sim 0.999$) and II ($R^2 \sim 0.981$), corresponding to A_g^1, A_g^2, A_g^3, A_g^8, A_g^9, and B_g^6 modes, respectively, according to Fig. 2(a) and Table I. The three extremely weak peaks at ∼50, 84, and 92 cm^{-1} (U1, U2, and U3) are difficult to identify due to the lack of experimental evidence and interference from dense phonon modes.

A. In-plane phonon and EPC anisotropies in $Bi_2Rh_3Se_2$

Figure 3(a) shows the 3D colormap surfaces with the projection of the normalized I according to the ARPRS spectra of $Bi_2Rh_3Se_2$ under 532 and 633 nm excitation in a parallel polarization configuration, respectively. The polarization angle (θ) is defined as 0° when the incident polarization is aligned with the black solid arrow in Fig. 1(c). The I of the phonon modes varies periodically with θ, indicating in-plane phonon anisotropy. For clarity, the extracted I of the corresponding mode is plotted in Figs. 3(b) and S3 [38]. According to the classical Placzek approximation [41], I is proportional to $|e_i \cdot R \cdot e_s^\tau|^2$, where R is the Raman tensor, and e_i and e_s are the unit polarization vectors of incident and scattering light, respectively. $e_i = e_s = (\cos\theta,\ \sin\theta,\ 0)$ in a parallel polarization configuration. Raman tensors of the A_g and B_g modes in $Bi_2Rh_3Se_2$ are expressed as

$$R_{A_g} = \begin{pmatrix} ue^{i\varphi_u} & de^{i\varphi_d} & 0 \\ de^{i\varphi_d} & ve^{i\varphi_v} & 0 \\ 0 & 0 & we^{i\varphi_w} \end{pmatrix}, \quad (2)$$

$$R_{B_g} = \begin{pmatrix} 0 & fe^{i\varphi_f} & 0 \\ fe^{i\varphi_f} & 0 & 0 \\ 0 & 0 & 0 \end{pmatrix}, \quad (3)$$

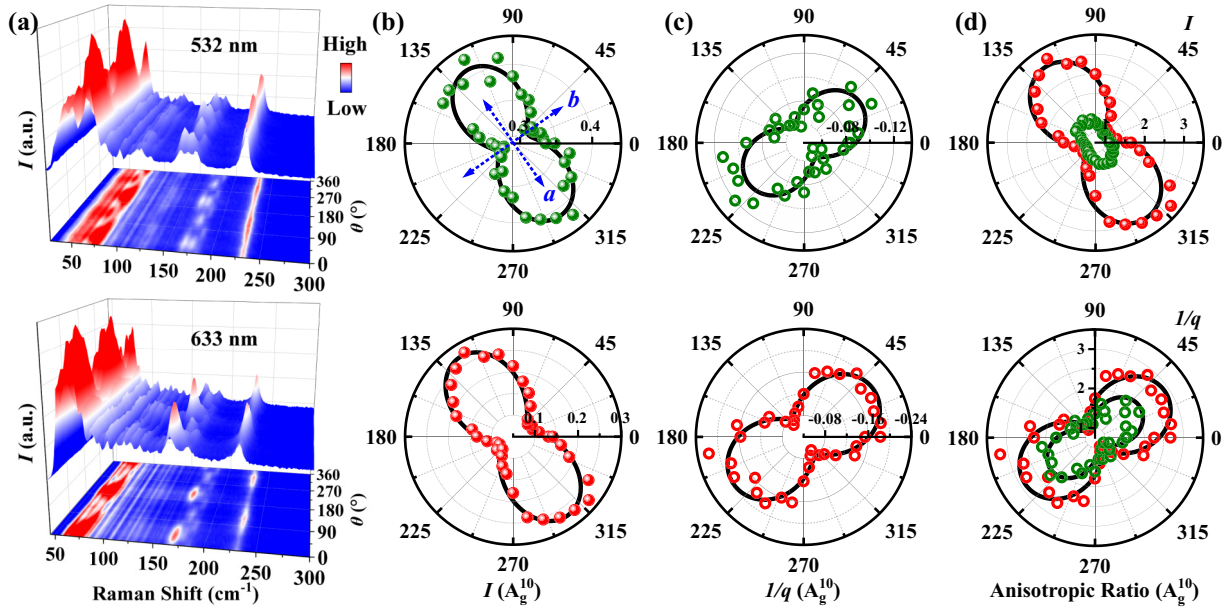

FIG. 3. (a) 3D colormap surfaces with the projection of ARPRS spectra of as-grown $Bi_2Rh_3Se_2$ crystal under 532 and 633 nm excitation in parallel polarization configuration. Polar plots of I (b), $1/q$ (c), and corresponding anisotropic ratios ($\frac{\text{the absolute value}}{\text{the absolute minimum value}}$) (d) for A_g^{10} mode. Solid lines are performed curves. Green and red dots represent 532 and 633 nm excitation, respectively. The extracted experimental data in (c) and (d) are fitted by a function of $a_1\sin\theta + a_2\cos\theta$.

where u, v, w, d, and f are Raman tensor elements, and φ is the phase of the Raman tensor element. I is associated with A_g and B_g modes in a parallel polarization configuration, which are written as

$$I_{A_g} = u^2\cos^4\theta + v^2\sin^4\theta + 4d^2\sin^2\theta\cos^2\theta + 4ud\cos^3\theta\sin\theta\cos\varphi_{ud} + 4vd\sin^3\theta\cos\theta\cos\varphi_{vd} + 2uv\sin^2\theta\cos^2\theta\cos 2\varphi_{uv}, \quad (4)$$

$$I_{B_g} = f^2\sin^2 2\theta, \quad (5)$$

where $\varphi_{ud} = \varphi_u - \varphi_d$, $\varphi_{vd} = \varphi_v - \varphi_d$, $\varphi_{uv} = \varphi_u - \varphi_v$. The polar plots of I in Figs. 3(b) and S3 [38] are performed well by Eqs. (4) and (5). The B_g^6 mode shows a four-lobed shape with intensity maxima at ~82°, 172°, 262°, and 352° regardless of excitation wavelength. Under 532 and 633 nm excitation, the A_g^3, A_g^8, and A_g^{10} modes all show a bow-tie-like shape. The intensity maxima of A_g^3 and A_g^8 modes are along ~ 37° (217°) (b-axis), and the intensity maximum of A_g^{10} mode is along ~ 127° (307°) (a-axis). Interestingly, under 532 nm excitation, the A_g^1, A_g^2, and A_g^9 modes show a propeller-shaped pattern with two intensity maxima along the b- and a-axes, respectively. Under 633 nm excitation, all still maintain a propeller-shaped pattern, but they show a secondary maximum in the normal direction of the corresponding intensity maximum, revealing excitation-wavelength-dependent polarization responses for A_g^1, A_g^2, and A_g^9 modes.

It has been reported that the polarizations of certain phonon modes are modified by optical birefringence, interference effects, and EPC when the excitation wavelength is changed in anisotropic materials [15,16,27,42–44]. The measured $Bi_2Rh_3Se_2$ crystal is hundreds of microns thick (much larger than the excitation wavelength) and is put on copper tape. Thus, the excitation-wavelength dependent EPC is most likely the determinant factor for the anomalous polarizations of A_g^1, A_g^2, and A_g^9 modes in $Bi_2Rh_3Se_2$, while the optical birefringence and interference effects may play a minor role and can be ignored [44]. Excitation wavelength-dependent EPCs have been directly and widely observed by ARPRS [15,22,23,42]. We adopt the semiquantitative analysis of $1/q$ to investigate the excitation-wavelength dependence of EPC in $Bi_2Rh_3Se_2$.

Figure 3(c) plots the $1/q$ of the A_g^{10} mode under 532 and 633 nm excitation, respectively. Under both excitations, $1/q$ varies with θ in a bow-tie-like mode, revealing the EPC anisotropy. Surprisingly, the intensity maximum of $1/q$ is along the b-axis, perpendicular rather than parallel to the I intensity maximum of the A_g^{10} mode (a-axis). This anomaly seems to indicate that EPC tends to inhibit I in $Bi_2Rh_3Se_2$, similar to the case in superconducting Nd(O, F)BiS_2 [22], but contrary to the fact that EPC is the dominant contributor to the I of the A_g mode in black phosphorus when the optical effects can be ignored [15,42]. Along the b-axis, the absolute value of $1/q$ excited by 633 nm (~0.20) is about twice that excited by 532 nm (~0.10), indicating a stronger EPC under 633 nm excitation. A decrease in the strength of EPC with increasing excitation photon energy has been observed in other superconductors [22]. To compare the relative strengths of I and $1/q$ for the A_g^{10} mode under 532 and 633 nm excitation, the anisotropic ratios ($\frac{\text{the absolute value}}{\text{the absolute minimum value}}$) of I and $1/q$ as a function of θ were compared quantitatively, as shown in Fig. 3(d). The ratios of both I and $1/q$ under 633 nm excitation are larger than those under 532 nm excitation, indicating stronger in-plane anisotropy under 633 nm excitation. Extracting reliable parameters of EPC from A_g^1, A_g^2, and A_g^9 modes in the future may make the analysis more rigorous.

B. Multiple CDW orders in $Bi_2Rh_3Se_2$

To investigate the temperature evolution of $Bi_2Rh_3Se_2$ phonons, the single-crystal TDRS (no polarizer) and TDXRD [along the (0,0,L) direction] measurements were performed from 80 to 300 K. The TDRS results are reversible during cooling-down and warming-up cycles at different incident polarizations, as shown in Fig. S4 [38]. A cooling cycle of TDRS measurement (incident polarization along the b-axis) is shown in Fig. 4(a). The Raman spectrum at 300 K (above T_s) is substantially different from that at 80 K (below T_s), indicating that phase transitions have occurred. Figure 4(b) shows the second derivative image of Fig. 4(a), where two distinct phase transitions are clearly observed at ~170 ± 10 K (T_1) and ~250 ± 10 K (T_2). Around T_2, the A_g^9 mode disappears, and a slight mode change at ~125 cm^{-1} can also be observed (zoom-in Raman spectra; see Fig. S5 [38]), which corresponds to the widely reported phase transition at T_s ~ 240 K in $Bi_2Rh_3Se_2$ [11–14], demonstrating the existence of a symmetry-breaking phase below T_2. Sakamoto *et al.* and Chen *et al.* have performed a systematic powder TDXRD study in $Bi_2Rh_3Se_2$, and only one additional diffraction peak was found in their respective results [11,14]. Figures S6(a)–(f) show the complete data and the zoomed-in diffraction peaks of (002), (004), (006), (008), and (0010) of $Bi_2Rh_3Se_2$ from our single-crystal TDXRD results, which do not reflect the apparent difference in the unit-cell parameter c with a temperature increase [38]. The extracted peak positions of (008) and (0010) peaks in Figs. S7(a) and (b) only display two slight changes at T_1 and T_2, respectively, well consistent with the TDRS results [38]. Our TDXRD measurements indicate that $Bi_2Rh_3Se_2$ does not undergo a structural phase transition like $Bi_2Rh_3S_2$ [45]. The optical conductivity measurement indicates the formation of an energy gap with associated spectral change only at low energies in $Bi_2Rh_3Se_2$, supporting a CDW transition at 240 K [12]. ARPES measurement observes the temperature dependence of the electronic structures in $Bi_2Rh_3Se_2$ and reveals CDW-induced band folding, band splitting, and the opening of the CDW gaps at and away from the Fermi level [13]. Thus, a pure structural phase transition is not supported in $Bi_2Rh_3Se_2$. A similar Raman temperature dependence for a CDW transition has been observed in $TaSe_3$ [46]. Therefore, the phase transition around T_2 is considered to be a CDW transition [11–13].

As the temperature decreases further below T_1, in region I, the A_g^1 and A_g^2 modes merge into a continuum (C1) broadly centered at ~62 cm^{-1}, and U1 blueshifts to ~55 cm^{-1} as a shoulder. For details, see the zoomed-in spectra in Fig. 4(c) and the analysis of selected peaks in Fig. S8 [38]. Another obvious change can be observed in region II and in the corresponding zoomed-in spectra in Fig. 4(d). All of the Raman

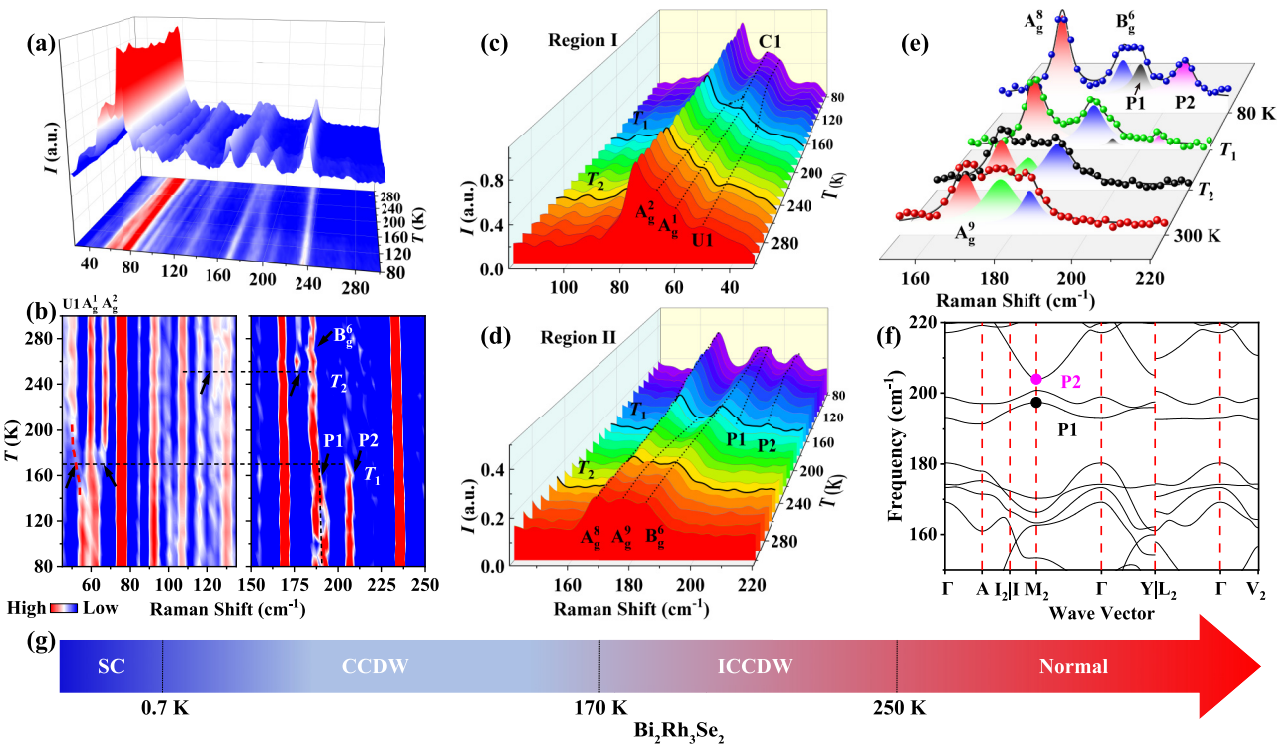

FIG. 4. (a) 3D colormap surface with the projection of unpolarized TDRS measurements of as-grown $Bi_2Rh_3Se_2$ crystal under 532 nm excitation. (b) Second derivative image of panel (a). Zoomed-in spectra of regions I (c) and II (d) in the cooling-down cycle. (e) Selected peak analysis based on BWF function at 80 K, T_1, T_2, and 300 K. (f) Zoomed-in calculated phonon dispersion from 150 to 220 cm^{-1}. (g) Phase diagram of $Bi_2Rh_3Se_2$ as a function of temperature.

peaks increase drastically with I, and two additional asymmetric peaks named $P1$ and $P2$ appear at ∼192 and 207 cm^{-1}, respectively, below T_1 [peaks fitting is shown in Fig. 4(e)], indicating that there is another symmetry-breaking phase at lower temperatures. The above observations confirm that another phase transition occurs at T_1, which has never been reported before.

Quantitative analysis of the Raman modes in region II is used to distinguish the two symmetry-breaking phases, as shown in Fig. 4(e). At 80 K, both $P1$ and $P2$ show asymmetric line shapes with the extracted q of ~ -5 and -3, respectively, suggesting EPC. Our previous ARPES report [13] has revealed that $Bi_2Rh_3Se_2$ is in a 2×2 CCDW phase at 30 K, leading to a BZ reconstruction. Unfortunately, the threshold temperature for the CCDW phase transition could not be determined directly, due to the limited experimental resolution [13]. Due to the BZ reconstruction, the phonon modes are folded from the M_2 point to the central Γ point (reconstructed BZ; see Fig. S9 [38]). Some of them exhibiting Raman activity could be assigned to the newly observed Raman peaks (such as $P1$ and $P2$). $P1$ and $P2$ are assigned to the two folded phonon modes of those at ∼197 and 204 cm^{-1} at the M_2 point, highlighted by black and magenta dots, respectively, in Fig. 4(f). Both $P1$ and $P2$ begin to appear at T_1, indicating that the 2×2 CCDW reconstruction exists below T_1. Coincidentally, Lin *et al.* reported that a CDW amplitude mode in $Bi_2Rh_3Se_2$ can be observed only below 170 K (T_1) [12]. Above T_1, the decrease of I in region II and the disappearance of $P1$ and $P2$ are similar to the observations of the CCDW to ICCDW transition in $TaSe_2$ and TaS_2, etc., possibly due to the loss of translation symmetry of the lattice in the ICCDW phase [25,47]. Thus, it seems that $Bi_2Rh_3Se_2$ has an ICCDW phase from T_1 to T_2. Conclusively, the phase diagram of $Bi_2Rh_3Se_2$ is proposed in Fig. 4(g).

CDW transitions typically result in an abnormal ω shift and I decrease of the phonon modes in Raman measurements, providing clear evidence for EPC [48–50]. Figure 5(a) emphasizes the temperature dependence of the extracted I (after background subtraction) of the CCDW-related $P1$ and $P2$. For both modes, I varies nonlinearly with increasing temperature and decays rapidly at $\sim T_1$. According to Landau theory of second-order phase transitions, taking the CDW gap as the order parameter (η), the temperature dependence of η can be written as [27,49–51]

$$\eta \sim \left(1 - \frac{T}{T_{\mathrm{CDW}}}\right)^{\beta}, \tag{6}$$

where β is the critical exponent. The temperature dependence of the Raman mode characteristic parameters X ($X = I, F$, and ω, etc.) is proportional to the square of η [52]. If the interactions of multiple CDWs are neglected [50], their temperature dependence is

$$X(T) = X_0 + A_i\left(1 - \frac{T}{T_{\mathrm{CDW}i}}\right)^{2\beta} \quad (i = 1, 2, 3, \ldots), \tag{7}$$

where X_0 is a temperature-independent constant and A_i is a coupling constant. The solid fitting curves using Eq. (7)

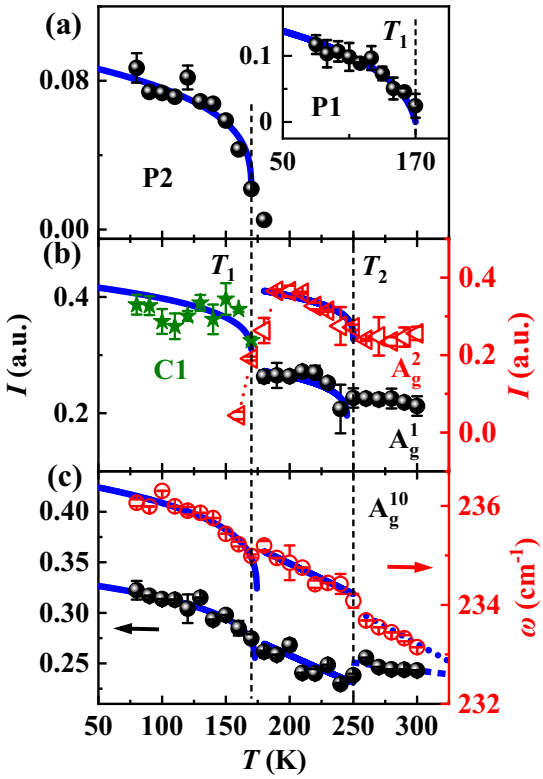

FIG. 5. Temperature-dependent I of the $P2$ (a), the $P1$ (inset), as well as $C1$, A_g^1, and A_g^2 modes (b). (c) Temperature-dependent I and ω of A_g^{10} mode. The solid lines are fitting curves using Eq. (7).

in Fig. 5(a) and the inset agree well with the experimental data, and the T_{CCDW}^{P1} of ~173 K and T_{CCDW}^{P2} of ~170 K are excellently close to T_1. β of I of $P1$ and $P2$ are extracted to be $\beta_{T_{\mathrm{CCDW}}^{P1}}^{I} = 0.145$ and $\beta_{T_{\mathrm{CCDW}}^{P2}}^{I} = 0.147$, which are much smaller than the experimentally reported β of ~0.3 in $ErTe_3$ [50] and the ideal β of 0.5 [51], suggesting a more drastic change at T_1 in $Bi_2Rh_3Se_2$. Figure 5(b) shows the temperature dependence of I of the CCDW- and ICCDW-related phonon modes below ~70 cm^{-1} in region I. CCDW-related $C1$ splits into ICCDW-related A_g^1 and A_g^2 modes above T_1. The I of $C1$ (green stars) rapidly decays at ~T_1, and those of A_g^1 and A_g^2 modes (black dots and red triangles) display similar behaviors at ~T_2. Such decay can be basically described by Eq. (7).

Further analysis of the CDW-unrelated A_g^{10} mode is shown in Fig. 5(c). I and ω both shift discontinuously with temperature, and their slopes suddenly change at T_1 and T_2. Obviously, the anharmonicity effect cannot describe them. Following Eq. (7), the temperature dependence of I and ω is presented basically. All extracted important fitting parameters are summarized in Table S1 [38]. Note that both CDW-related and unrelated phonon modes change at T_1 and T_2. The underlying physical mechanism deserves further investigations. It implies that there is a coupling between electrons and phonons when the CCDW and ICCDW transitions occur in $Bi_2Rh_3Se_2$. In addition, the temperature dependence of EPC is observed semiquantitatively by q. The extracted q (<0) from A_g^{10} mode, as shown in Fig. S10(a) [38], unexpectedly increases from ~ -22 to ~ -12 above T_1, indicating that EPC is enhanced. The extracted q (<0) from A_g^3 mode shows clearly different values in CCDW, ICCDW, and normal phases, indicating that EPC is different in different phases in $Bi_2Rh_3Se_2$, as shown in Fig. S10(b) [38]. The above results reveal that EPC plays a vital role in the CDW transitions in $Bi_2Rh_3Se_2$.

III. CONCLUSION

We have performed systematic Raman scattering investigations on the single-crystal $Bi_2Rh_3Se_2$. ARPRS measurements that reveal the in-plane anisotropic phonons and EPC. A consistent physical picture of newly observed Raman peaks in TDRS measurements and the zone-folding of the phonon modes indicates that a 2×2 CCDW phase exists in $Bi_2Rh_3Se_2$ below ~170 K. Furthermore, an ICCDW phase exists from ~170 to ~250 K. Temperature-dependent q discloses different EPC in the above phases. Our findings suggest that $Bi_2Rh_3Se_2$ is a possible material to investigate the interaction between CDW and superconductivity.

IV. MATERIALS AND METHODS

A. Experimental section

High-quality $Bi_2Rh_3Se_2$ single crystals were grown by the self-flux method [11,13], whose crystallographic structure was examined by XRD (Rigaku Smartlab) and HRTEM (jeol2100f). TDXRD measurements were performed at special temperatures in a warming cycle. All Raman measurements were taken at an InVia Qontor system (Renishaw, UK) with an 1800 lines/mm grating in the backscattering configuration under 532 and 633 nm laser excitation with a spot size less than 1 μm. The laser power was kept low enough to avoid the heating effect. The ARPRS measurements were performed from 0° to 360° with a step of 15° at room temperature. The TDRS measurements were taken from 80 to 300 K with a step of 10 K using the Raman spectroscope combined with a variable temperature sample manipulator (Linkam THMS600, UK) with 0.01 K accuracy and stability. All experiments were performed on the freshly cleaved samples, and all temperature-dependent Raman data were normalized by a divided intensity of A_g^3 (~75 cm^{-1}) mode at 80 K. The I of ARPRS in Fig. S3 is extracted by a Lorentzian function. In regions I and II, the peaks are very close to each other and change substantially with polarization angle θ, resulting in complications in resolving individual Raman-active modes and difficulty in extracting reliable q using the BWF function. It is reported that such regions being performed with a sum of Lorentzian functions can simplify the problem, although EPC presents [27,53]. For TDRS, the spectral ranges to fit the isolated A_g^{10} mode, regions I and II, with Fano functions are taken in the range of 200–260, 45–100, and 150–220 cm^{-1}, respectively.

B. DFPT calculations

The force constants of all atoms in the normal state are determined using VASP. In calculated dynamical properties, we include contributions from cubic interatomic force constants to phonon frequencies. Phonon calculations were performed in the supercell with 56 atoms containing $2 \times 2 \times 2$ conventional unit cells. The phonon-dispersion curves and phonon density of states (DOS) are calculated using PHONOPY software.

ACKNOWLEDGMENTS

We acknowledge the financial support from the National Natural Science Foundation of China (Grants No. 11874427 and No. 12074436). J.-Q.M. would like to acknowledge support from the science and technology innovation program of Hunan Province (2022RC3068). This work was carried out in part using computing resources at the High Performance Computing Center of Central South University.

[1] G. Ghiringhelli, A. Frano, B. Keimer, C. Mazzoli, D. Peets, D. Hawthorn, E. Schierle, E. Weschke, F. He, G. Sawatzky *et al.*, Science **337**, 821 (2012).

[2] G. Campi, A. Bianconi, N. Poccia, G. Bianconi, L. Barba, G. Arrighetti, D. Innocenti, J. Karpinski, N. D. Zhigadlo, S. M. Kazakov *et al.*, Nature (London) **525**, 359 (2015).

[3] S. Gerber, H. Jang, H. Nojiri, S. Matsuzawa, H. Yasumura, D. Bonn, R. Liang, W. Hardy, Z. Islam, A. Mehta *et al.*, Science **350**, 949 (2015).

[4] X. Teng, L. Chen, F. Ye, E. Rosenberg, Z. Liu, J.-X. Yin, Y.-X. Jiang, J. S. Oh, M. Z. Hasan, K. J. Neubauer *et al.*, Nature (London) **609**, 490 (2022).

[5] J. Bardeen, L. N. Cooper, and J. R. Schrieffer, Phys. Rev. **108**, 1175 (1957).

[6] R. Peierls and R. E. Peierls, *Quantum Theory of Solids* (Oxford University Press, Oxford, 1955).

[7] S.-K. Chan and V. Heine, J. Phys. F **3**, 795 (1973).

[8] T. Kiss, T. Yokoya, A. Chainani, S. Shin, T. Hanaguri, M. Nohara, and H. Takagi, Nat. Phys. **3**, 720 (2007).

[9] I. Vinograd, R. Zhou, M. Hirata, T. Wu, H. Mayaffre, S. Krämer, R. Liang, W. Hardy, D. Bonn, and M.-H. Julien, Nat. Commun. **12**, 3274 (2021).

[10] J. Chang, E. Blackburn, A. Holmes, N. B. Christensen, J. Larsen, J. Mesot, R. Liang, D. Bonn, W. Hardy, A. Watenphul *et al.*, Nat. Phys. **8**, 871 (2012).

[11] T. Sakamoto, M. Wakeshima, Y. Hinatsu, and K. Matsuhira, Phys. Rev. B **75**, 060503(R) (2007).

[12] T. Lin, L. Y. Shi, Z. X. Wang, S. J. Zhang, Q. M. Liu, T. C. Hu, T. Dong, D. Wu, and N. L. Wang, Phys. Rev. B **101**, 205112 (2020).

[13] Z.-T. Liu, C. Zhang, Q.-Y. Wu, H. Liu, B. Chen, Z.-B. Yin, S.-T. Cui, Z. Sun, S.-X. Zhu, J.-J. Song *et al.*, Sci. China-Phys. Mech. Astron. **66**, 277411 (2023).

[14] C. Chen, C. Chan, S. Mukherjee, C. Chou, C. Tseng, S. Hsu, M.-W. Chu, J.-Y. Lin, and H. Yang, Solid State Commun. **177**, 42 (2014).

[15] N. Mao, X. Wang, Y. Lin, B. G. Sumpter, Q. Ji, T. Palacios, S. Huang, V. Meunier, M. S. Dresselhaus, W. A. Tisdale *et al.*, J. Am. Chem. Soc. **141**, 18994 (2019).

[16] Y. Wang, F. Chen, X. Guo, J. Liu, J. Jiang, X. Zheng, Z. Wang, M. M. Al-Makeen, F. Ouyang, Q. Xia *et al.*, J. Phys. Chem. Lett. **12**, 10753 (2021).

[17] F. Cerdeira, T. A. Fjeldly, and M. Cardona, Phys. Rev. B **8**, 4734 (1973).

[18] M. Balkanski, K. Jain, R. Beserman, and M. Jouanne, Phys. Rev. B **12**, 4328 (1975).

[19] J. M. Atkin, S. Berweger, E. K. Chavez, M. B. Raschke, J. Cao, W. Fan, and J. Wu, Phys. Rev. B **85**, 020101(R) (2012).

[20] Y. Wang, X. Guo, S. You, J. Jiang, Z. Wang, F. Ouyang, and H. Huang, Nano Res. **16**, 1115 (2023).

[21] S. Zhu and W. Zheng, J. Phys. Chem. Lett. **12**, 5261 (2021).

[22] S. F. Wu, P. Richard, X. B. Wang, C. S. Lian, S. M. Nie, J. T. Wang, N. L. Wang, and H. Ding, Phys. Rev. B **90**, 054519 (2014).

[23] A.-M. Zhang and Q.-M. Zhang, Chin. Phys. B **22**, 087103 (2013).

[24] X. Xi, L. Zhao, Z. Wang, H. Berger, L. Forró, J. Shan, and K. F. Mak, Nat. Nanotechnol. **10**, 765 (2015).

[25] R. Samnakay, D. Wickramaratne, T. Pope, R. Lake, T. Salguero, and A. Balandin, Nano Lett. **15**, 2965 (2015).

[26] S. J. Sandoval, X. K. Chen, and J. C. Irwin, Phys. Rev. B **45**, 14347 (1992).

[27] R. Singha, S. Samanta, T. S. Bhattacharya, S. Chatterjee, S. Roy, L. Wang, A. Singha, and P. Mandal, Phys. Rev. B **102**, 205103 (2020).

[28] D. L. Duong, G. Ryu, A. Hoyer, C. Lin, M. Burghard, and K. Kern, ACS Nano **11**, 1034 (2017).

[29] O. R. Albertini, R. Zhao, R. L. McCann, S. Feng, M. Terrones, J. K. Freericks, J. A. Robinson, and A. Y. Liu, Phys. Rev. B **93**, 214109 (2016).

[30] J. Shi, X. Chen, L. Zhao, Y. Gong, M. Hong, Y. Huan, Z. Zhang, P. Yang, Y. Li, Q. Zhang *et al.*, Adv. Mater. **30**, 1804616 (2018).

[31] X. Wang, H. Liu, J. Wu, J. Lin, W. He, H. Wang, X. Shi, K. Suenaga, and L. Xie, Adv. Mater. **30**, 1800074 (2018).

[32] S. Li, E. Drueke, Z. Porter, W. Jin, Z. Lu, D. Smirnov, R. Merlin, S. D. Wilson, K. Sun, and L. Zhao, Phys. Rev. Lett. **125**, 087202 (2020).

[33] M. M. AL-Makeen, X. Guo, Y. Wang, D. Yang, S. You, M. Yassine, J. Jiang, P.-B. Song, Y.-G. Shi, H. Xie *et al.*, Phys. Status Solidi RRL **16**, 2200257 (2022).

[34] Z. Wang, Y. Wang, X. Guo, S. You, T. Niu, M. Zhong, Q. Xia, and H. Huang, Appl. Phys. Lett. **121**, 122106 (2022).

[35] $Bi_2Rh_3Se_2$ ($Rh_3Bi_2Se_2$) Crystal Structure: Datasheet from "PAULING FILE Multinaries Edition–2012," in SpringerMaterials, https://materials.springer.com/isp/crystallographic/docs/sd_1934275.

[36] Q. Zheng, P. Ren, Y. Peng, W. Zhou, Y. Yin, H. Wu, W. Gong, W. Wang, D. Tang, and B. Zou, J. Phys. Chem. Lett. **10**, 2182 (2019).

[37] F. Chen, J. Liu, X. Zheng, L. Liu, H. Xie, F. Song, Y. Gao, and H. Huang, Chin. Phys. B **29**, 116802 (2020).

[38] See Supplemental Material at http://link.aps.org/supplemental/10.1103/PhysRevB.108.045118 for structure characterization and Brillouin zone (BZ) of $Bi_2Rh_3Se_2$, polarizations of representative phonon modes in $Bi_2Rh_3Se_2$, temperature-dependent Raman and XRD measurements, temperature-dependent evolution of Raman peaks in region I, schematic of BZ 2×2 reconstruction, and extracted q as a function of temperature.

[39] G. Wertheim, M. Butler, K. West, and D. Buchanan, Rev. Sci. Instrum. **45**, 1369 (1974).

[40] U. Fano, Phys. Rev. **124**, 1866 (1961).

[41] R. Loudon, Adv. Phys. **13**, 423 (1964).

[42] X. Ling, S. Huang, E. H. Hasdeo, L. Liang, W. M. Parkin, Y. Tatsumi, A. R. Nugraha, A. A. Puretzky, P. M. Das, B. G. Sumpter *et al.*, Nano Lett. **16**, 2260 (2016).
[43] J. Kim, J.-U. Lee, J. Lee, H. J. Park, Z. Lee, C. Lee, and H. Cheong, Nanoscale **7**, 18708 (2015).
[44] D. Yoon, H. Moon, Y.-W. Son, J. S. Choi, B. H. Park, Y. H. Cha, Y. D. Kim, and H. Cheong, Phys. Rev. B **80**, 125422 (2009).
[45] U. S. Kaluarachchi, W. Xie, Q. Lin, V. Taufour, S. L. Bud'ko, G. J. Miller, and P. C. Canfield, Phys. Rev. B **91**, 174513 (2015).
[46] J. Ma, S. Nie, X. Gui, M. Naamneh, J. Jandke, C. Xi, J. Zhang, T. Shang, Y. Xiong, I. Kapon *et al.*, Nat. Mater. **21**, 423 (2022).
[47] S. L. L. M. Ramos, R. Plumadore, J. Boddison-Chouinard, S. W. Hla, J. R. Guest, D. J. Gosztola, M. A. Pimenta, and A. Luican-Mayer, Phys. Rev. B **100**, 165414 (2019).
[48] M. Lavagnini, M. Baldini, A. Sacchetti, D. Di Castro, B. Delley, R. Monnier, J.-H. Chu, N. Ru, I. R. Fisher, P. Postorino *et al.*, Phys. Rev. B **78**, 201101(R) (2008).
[49] M. Lavagnini, H.-M. Eiter, L. Tassini, B. Muschler, R. Hackl, R. Monnier, J.-H. Chu, I. R. Fisher, and L. Degiorgi, Phys. Rev. B **81**, 081101(R) (2010).
[50] N. Lazarević, Z. V. Popović, R. Hu, and C. Petrovic, Phys. Rev. B **83**, 024302 (2011).
[51] L. D. Landau and E. M. Lifshitz, *Statistical Physics: Volume 5* (Elsevier, Amsterdam, 2013).
[52] J. Petzelt and V. Dvorak, J. Phys. C **9**, 1571 (1976).
[53] D. Kumar, V. Kumar, R. Kumar, M. Kumar, and P. Kumar, Phys. Rev. B **105**, 085419 (2022).